Frontiers in Heat and Mass Transfer

Tech Science Press

DOI: 10.32604/fhmt.2023.041829

ARTICLE

Evaporation Heat Transfer Characteristics from a Sintered Powder Wick Structure Sandwiched between Two Solid Walls

Yasushi Koito[1,*], Shoma Hitotsuya[2], Takamitsu Takayama[2] and Kenta Hashimoto[2]

[1]Division of Industrial Fundamentals, Faculty of Advanced Science and Technology, Kumamoto University, Kumamoto, 860-8555, Japan

[2]Department of Mechanical and Mathematical Engineering, Graduate School of Science and Technology, Kumamoto University, Kumamoto, 860-8555, Japan

*Corresponding Author: Yasushi Koito. Email: koito@gpo.kumamoto-u.ac.jp

Received: 08 May 2023 Accepted: 07 July 2023 Published: 30 November 2023

ABSTRACT

An ultra-thin flattened heat pipe has been developed with a centered wick structure. This structure is essential to make the heat pipe thinner. However, the centered wick structure reduces the evaporation and condensation surface areas of the wick structure because it is sandwiched between heat pipe walls. In this study, because detailed discussion has not been made, heat transfer experiments were conducted for the wick structure sandwiched between two solid walls. This study focused on the evaporation heat transfer characteristics from the sandwiched wick structure. The experiments were conducted with three wick structures, that is, strip-shaped sintered copper powders with thicknesses of 0.5, 1.0, and 1.5 mm. Water was used as working fluid. The capillary pumping performance, that is, the liquid lifting velocities of the three wick structures were the same. The experimental results of the three wick structures were compared regarding the relation between the evaporation heat transfer rate and the superheat of the working fluid. The heat transfer experiments were also conducted when one of the solid walls was removed from the wick structure. It was confirmed that even if the wick structure was sandwiched between the solid walls, sufficient evaporation of the working fluid occurred from the thin sides of the wick structure.

KEYWORDS

Heat transfer; ultra-thin heat pipe; centered wick structure; restricted evaporation surface; thermal design; electronics cooling

Nomenclature

A	Cross-sectional area (m^2)
C	Specific heat (J/(kgK))
F	Capillary force (N)
G	Gravitational acceleration (m/s^2)
H	Height (mm, m)
h_{fg}	Latent heat (J/kg)
K	Permeability (m^2)

m	Mass (kg)
$\dot{m}$	Mass flow rate (kg/s)
P	Electrical power (W)
Q	Heat transport rate (W)
T	Temperature (°C)
T_{sat}	Saturation temperature (°C)
t	Time (s)
V	Volume (m^3)
w	Width (m)
X_1, X_2	Constant (m^2/s^2)

Greek Symbols

ΔT	Superheat (°C)
δ	Thickness (mm)
ε	Porosity (−)
η	Ratio defined by Eq. (8) (−)
μ	Viscosity (Pas)
ρ	Density (kg/m^3)

Superscript

´	Theoretical

Subscripts

1–8	Measurement point
c	Copper
e	Evaporation
f	Fluid
l	Liquid, left rod
max	Maximum
r	Right rod
s	Surface

1 Introduction

The capillary-driven heat pipe is a well-known traditional heat pipe, which has been widely used such as for electronics cooling (Tang et al. [1], Mochizuki et al. [2], Velardo et al. [3], Wang et al. [4], Zhao et al. [5]), LED heat sinks (Singh et al. [6], Pekur et al. [7], Tang et al. [8]), and battery thermal management (Behi et al. [9], Luo et al. [10]). The heat pipe transports heat from one end (evaporator section) to the other end (condenser section) without any power input. An appropriate amount of working fluid is enclosed in the heat pipe. Liquid evaporates at the evaporator section, and vapor flows to the condenser section, where the vapor condenses to condensate. Latent heat of the working fluid is utilized for heat transport. A capillary wick structure is placed in the heat pipe to pump the condensate back to the evaporator section. To date, many studies have been conducted on the capillary wick structure (e.g., Tang et al. [11], Weibel et al. [12], Weibel et al. [13], Deng et al. [14], Sudhakar et al. [15], Zhang et al. [16]), because that is an important component dominating the thermal performance of the heat pipe.

Recently, the ultra-thin flattened heat pipe has been developed for thermal management of thin electronics devices. Previous studies on the ultra-thin flattened heat pipe were already reviewed in the paper [17] presented by one of the authors. Besides these studies, Zhou et al. [18] proposed a hybrid spiral woven mesh wick structure, and conducted the experiment to study the effect of wick's weaving method on the thermal performance of ultra-thin heat pipes. Tang et al. [19] proposed a multiple mesh wick structure with oxidation treatment and sintering. They fabricated three ultra-thin heat pipes with thicknesses of 0.8, 1.0, and 1.2 mm, and investigated their thermal performance experimentally.

Typical cross sections of a traditional heat pipe and ultra-thin flattened heat pipe are shown in Fig. 1. In the traditional heat pipe [20], a wick structure is placed on the inner wall of the heat pipe container, and a vapor flow space is surrounded by the wick structure. Evaporation and condensation of the working fluid occur on the inner surface of the wick structure. In the ultra-thin flattened heat pipe [21–24], on the other hand, a wick structure is positioned at the center of the flattened heat pipe container, and vapor flow spaces are retained on both sides of the wick structure. Although ultra-thin flattened heat pipes with a wick layer were developed [25–27], this structure reduces the vapor flow space. Thus, the centered wick structure is essential to make the heat pipe thinner. However, the centered wick structure reduces the evaporation and condensation surface areas of the wick structure. That is, because the upper and lower surfaces of the wick structure are in contact with the inner walls of the container, the evaporation and condensation occur only on the sides of the wick structure. Moreover, because the heat pipe container is flattened, the side surface area of the wick structure is much smaller than the upper and lower surface areas. Therefore, in the ultra-thin flattened heat pipe, the evaporation and condensation surfaces are restricted to the thin side of the wick structure. Recently, a comb-like thin wick structure was developed for the ultra-thin flattened heat pipe [28–30]. However, this structure also reduces the evaporation and condensation surface areas of the wick structure because it is sandwiched between heat pipe walls.

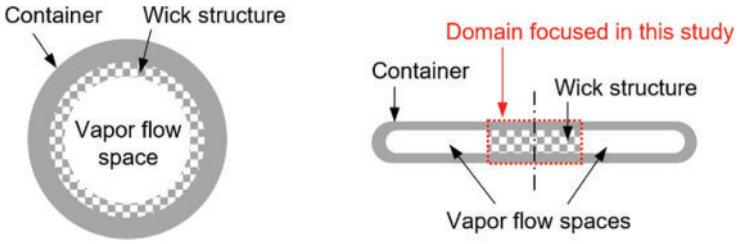

(a) Traditional heat pipe (b) Ultra-thin flattened heat pipe

Figure 1: Schematic diagram of the cross sections of heat pipes

To the authors' knowledge, sufficient discussion has not been made on the evaporation and condensation heat transfer characteristics of the wick structure sandwiched between solid walls. In this study, therefore, heat transfer experiments were conducted for the wick structure sandwiched between two solid walls. This study focused on the evaporation heat transfer characteristics from the sandwiched wick structure. The wick structure studied was a strip-shaped thin wick structure made of sintered copper powder. Water was employed as working fluid. Because the ultra-thin flattened heat pipe is becoming thinner, three wick structures with thicknesses of 0.5, 1.0, and 1.5 mm were prepared. Heat transfer experiments were also conducted when one of the solid walls was removed from the wick structure, and the results were compared with those obtained with the sandwiched wick structure.

2 Experimental Method and Conditions

Three strip-shaped wick structures with different thickness were made by sintering spherical copper powder in a furnace. The thickness, δ, of the wick structure was 0.5 mm, 1.0 mm, and 1.5 mm while they had the same length and width of 70 mm and 10 mm, respectively. Fig. 2 shows the particle size measurement result of the copper powder. The particle size was in the range of 50–300 μm, and the average was 132 μm. The porosity, ε, of the wick structure evaluated by the following equation was 50.2% on average:

$$\varepsilon = \frac{V - m/\rho_c}{V} \tag{1}$$

where V and m are the volume and mass of the wick structure, respectively. ρ_c is the density of copper. The above-mentioned 50.2% was obtained by repeating the fabrication and measurement of the wick structure five times.

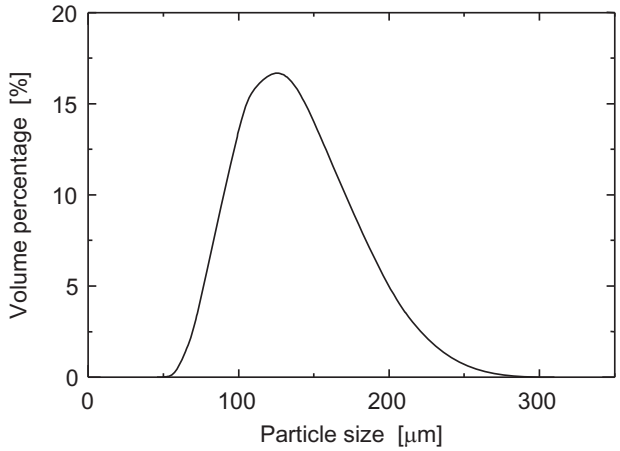

Figure 2: Particle size distribution of the copper powder

Fig. 3 shows the schematic diagram of the experimental apparatus. The wick structure was placed vertically, and the upper 10 mm of the wick structure was sandwiched between two rectangular brass rods. The cross section of these rods was 10 mm × 10 mm. A cartridge heater was inserted into the left end of the left rod, and the heater was connected to a wattmeter and a power supply. The lower 10 mm of the wick structure was placed in working fluid in a beaker. A water jacket and a thermostatic bath were employed to control the temperature of the working fluid in the beaker. A knob bolt and a load cell were used to adjust the pressure sandwiching the wick structure. A lab jack was used to adjust the liquid lifting height, which was the height from the surface of the working fluid in the beaker to the lower surface of the rods. For temperature measurement, 0.5-mm-diameter thermocouples were used at each position shown in Fig. 4. Regarding T_1–T_8, small holes of 0.6 mm in diameter and 5 mm in depth were drilled at each position, and the thermocouples were inserted there. The thermocouple was also used to measure the temperature, T_f, of the working fluid in the beaker. The thermocouples and load cell were connected to a data logger to record the temperature and pressure data. Except for the ends of each rod close to the wick structure, the two rods were covered with a thermal insulation material to reduce heat loss.

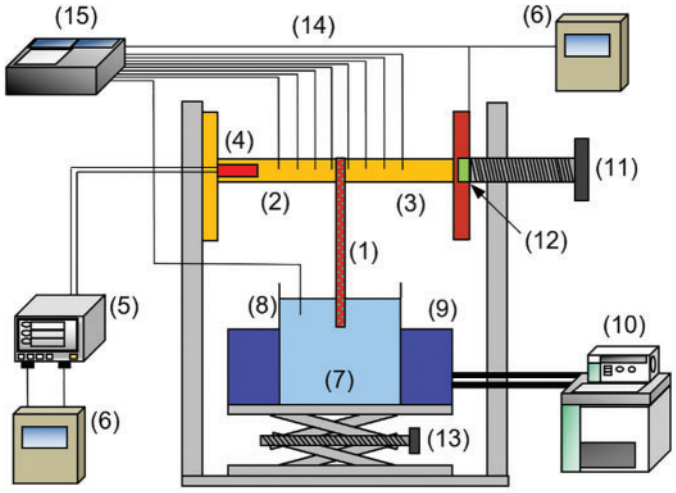

(1) Wick structure
(2) Left rod
(3) Right rod
(4) Heater
(5) Wattmeter
(6) Power supply
(7) Working fluid
(8) Beaker
(9) Water jacket
(10) Thermostatic bath
(11) Knob bolt
(12) Load cell
(13) Lab jack
(14) Thermocouple
(15) Data logger

Figure 3: Schematic diagram of the experimental apparatus (Exp-1)

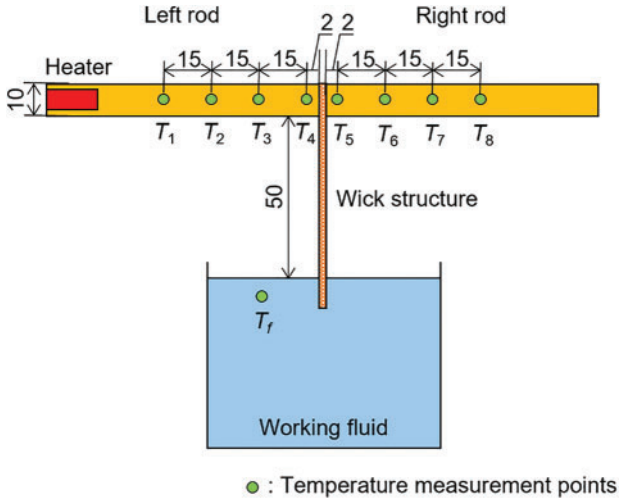

Figure 4: Temperature measurement points (Exp-1)

Two kinds of experiments (Exp-1 and Exp-2) were conducted. In Exp-1, because the ultra-thin flattened heat pipe is becoming thinner, 0.5, 1.0, and 1.5-mm-thick wick structures were used, and their evaporation heat transfer characteristics were compared. Each wick structure was sandwiched between the brass rods as shown in Figs. 3 and 4. In Exp-2, two kinds of additional components (Type A and Type B) were used, and each was placed between the wick structure and the right rod as shown in Fig. 5. The 1.0-mm-thick wick structure was employed. Type A and Type B components were used

to compare the evaporation heat transfer characteristics under the two cases: the wick structure was sandwiched between the two rods and the right rod was removed from the wick structure. When the right rod was removed, the evaporation surface area of the wick structure was much increased, and Type B was used to fix the wick structure onto the left rod. Type B had a vapor channel, which enabled the evaporation from the right surface of the wick structure. Since the vapor channel of Type B was made of polycarbonate, and the generated vapor flowed out from the vapor channel, the heat was hardly transferred from the wick structure to the right rod. To meet this condition, a Bakelite block with low thermal conductivity was used as Type A, which hardly transferred the heat as well from the wick structure to the right rod.

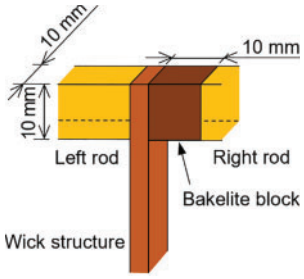

(a) Exp-2 with Type A component

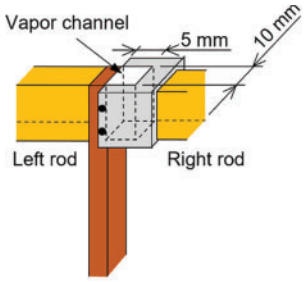

(b) Exp-2 with Type B component

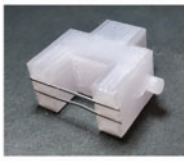

(c) Photograph of Type B component

Figure 5: Use of additional components in Exp-2

In each experiment, after T_f was adjusted at 20°C, the upper 10 mm of the wick structure was heated with the heater through the left rod. The upper 10 mm is termed an evaporator section in this paper. Temporal changes in the temperatures of T_1 to T_8 were recorded, and the temperature distributions in the rods at steady state were obtained. The electrical power, P, to the heater was increased stepwise, and the heating was terminated when T_1 to T_4 continued to rise. The liquid lifting height was set at 50 mm, and the pressure sandwiching the wick structure was adjusted at 0.5 MPa. Water was used as the working fluid. According to the guide to the expression of uncertainty in measurement [31], the uncertainties for the temperatures and electrical power were 0.58°C and 0.12 W, respectively.

3 Results and Discussion

3.1 Capillary Pumping Performance

Before conducting the experiments to investigate the evaporation heat transfer characteristics, the capillary pumping performance of the three wick structures was evaluated experimentally. In

this experiment, the wick structure was placed vertically, and water was used as the working fluid. The experiment was started by soaking the lower 10 mm of the wick structure in the working fluid maintained at 20°C, and the temporal change in the height, h, of the liquid surface rising in the wick structure was measured. Based on the previous study conducted by Tang et al. [11], the height was measured by using an IR camera. Fig. 6 shows the temporal changes in h for the 0.5, 1.0, and 1.5-mm-thick wick structures. The horizontal axis is the time, t, after soaking the wick structure in the working fluid. As expected, the h value started to increase immediately after the wick structure was soaked, and the change in h became smaller with increasing t. Differences were hardly found in the results for $\delta = 0.5$, 1.0, and 1.5 mm, which confirmed that the capillary pumping performance of the three wick structures was the same.

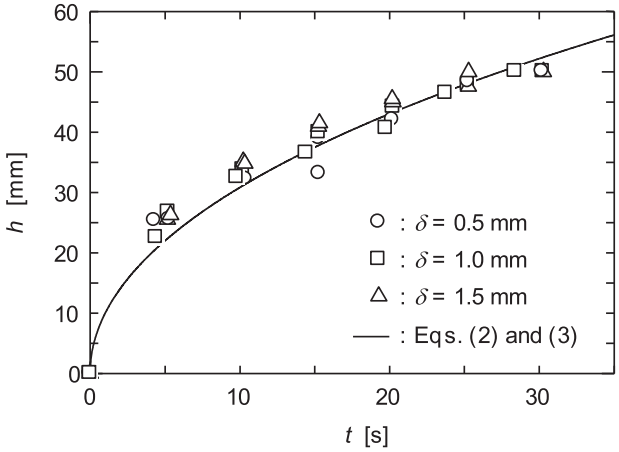

Figure 6: Capillary pumping performance of the wick structures

Using the experimental results, the following empirical equation was obtained regarding the relation between h and t.

$$\frac{d}{dt}\left(h\frac{dh}{dt}\right) = X_1 - X_2 h\frac{dh}{dt} - hg, X_1 = 3.33, X_2 = 6.59 \times 10^4 \tag{2}$$

where g is the gravitational acceleration. The derivation process of Eq. (2) is described in Appendix. The initial condition for this equation was expressed as

$$h = \frac{dh}{dt} = 0 \text{ at } t = 0 \tag{3}$$

The numerical result of Eq. (2) with Eq. (3) is also shown in Fig. 6. Eqs. (2) and (3) were employed to evaluate the dh/dt value, which is required in the following section.

3.2 Heat Transfer Characteristics: Exp-1

From the temperature distributions obtained in the experiments, the heat transfer rates through the left, Q_l, and right, Q_r, rods were evaluated by using Fourier's law. Q_l was obtained from T_1 to T_4, while T_5 to T_8 were used to calculate Q_r. The evaporation heat transfer rate, Q_e, of the working fluid was then obtained by

$$Q_e = Q_l - Q_r \tag{4}$$

According to the guide to the expression of uncertainty in measurement [31], the uncertainty for the heat transfer rate was 0.25 W. Besides, the surface temperature, T_s, of the left rod in contact with the wick structure was evaluated by extrapolating T_1 to T_4, and the superheat, ΔT, was defined by

$$\Delta T = T_s - T_{sat} \tag{5}$$

where T_{sat} is the saturation temperature of the working fluid corresponding to the pressure acting on the working fluid. Since the present experiments were conducted under atmospheric pressure, T_{sat} was almost 100°C.

Fig. 7 shows the ΔT value at each P for the 1.0-mm-thick wick structure. The working fluid at 20°C was pumped from the bottom to the top (evaporator section) of the wick structure. When P was 25 and 30 W, the temperature of the working fluid did not increase to T_{sat}, and thus ΔT showed a negative value. When P was increased to 35 W, T_s became larger than T_{sat}. Because the evaporation of the working fluid occurred at the evaporator section, an increment in ΔT with P was relatively small in 35 W $\leq P \leq$ 55 W. In this range, although the evaporation rate of the working fluid increased with increasing P, sufficient liquid was supplied to the evaporator section by the action of capillary force. However, when P was increased to 60 W, the increment in ΔT became larger because the liquid supply to the evaporator section was insufficient. This result implies that the wick structure encountered a capillary limit, and heat conduction was dominant in the wick structure. As shown by dotted lines in Fig. 7, except for the experimental results at $P = 25$ and 30 W, the relations between ΔT and P before (35 W $\leq P \leq$ 55 W) and after (60 W $\leq P \leq$ 80 W) the capillary limit were extrapolated respectively, and the P value at their intersection was obtained as a maximum electrical power. This maximum power is represented by P_{max} and indicated in the figure. Besides, the Q_e value at P_{max} was defined as a maximum heat transfer rate, $Q_{e,max}$.

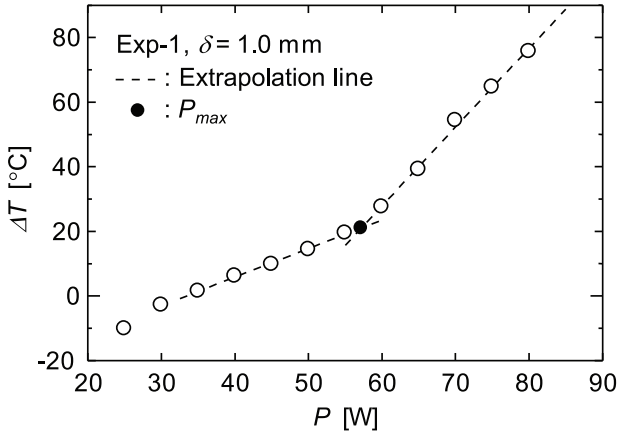

Figure 7: Evaporation heat transfer characteristics of the 1.0-mm-thick wick structure (Exp-1)

Fig. 8 shows the ΔT values at each Q_e for the 0.5, 1.0, and 1.5-mm-thick wick structures. The maximum heat transfer rates, $Q_{e,max}$, for the three wick structures are also shown in this figure. Because the cross-sectional area of the wick structure is proportional to δ, the flow rate of liquid supplied to the evaporator section increases with increasing δ. Thus, the $Q_{e,max}$ value became larger with increasing δ although the capillary pumping performance, that is, the liquid lifting velocities of the three wick structures were the same. Since the wick structure was sandwiched by the brass rods, the evaporation surface area of the wick structure for $\delta = 0.5$ mm was half the area for $\delta = 1.0$ mm. However, the ΔT values for the two wick structures were found to be almost the same. This agreement implies that the

evaporation of the working fluid from the thin sides of the wick structure was ensured although δ was reduced from 1.0 mm to 0.5 mm. The evaporation thermal resistances were almost the same for the 0.5 and 1.0-mm-thick wick structures. Moreover, it was also found that, except for ΔT at $Q_e = 17.4$ and 18.9 W, the ΔT value for the 1.5-mm-thick wick structure was smaller than those for the 0.5 and 1.0-mm-thick wick structures. This is because of the occurrence of boiling in the wick structure.

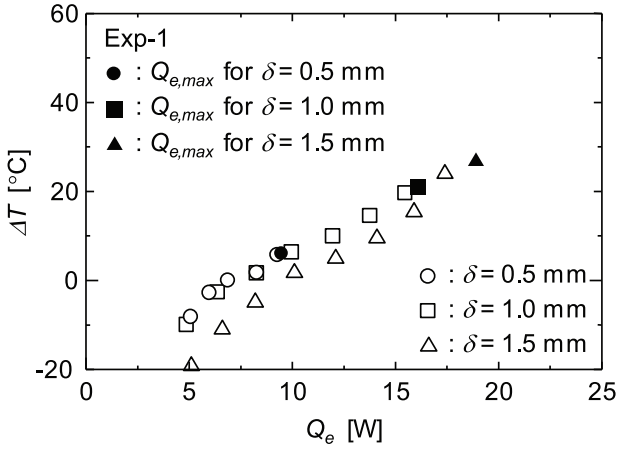

Figure 8: Comparison between the evaporation heat transfer characteristics for the 0.5, 1.0, and 1.5-mm-thick wick structures (Exp-1)

Using the velocity of the rising liquid surface, dh/dt, evaluated by Eqs. (2) and (3), the maximum mass flow rate of the liquid, $\dot{m}_{l,max}$, pumped to the evaporator section was estimated by

$$\dot{m}_{l,max} = \rho_l w \delta \varepsilon \left.\frac{dh}{dt}\right|_{h=50\text{mm}} \tag{6}$$

where ρ_l is the liquid density, w the width of the wick structure. Since the liquid lifting height was 50 mm in the present experiments, the dh/dt value was evaluated at $h = 50$ mm. The theoretical maximum heat transfer rate, $Q'_{e,max}$, was calculated by

$$Q'_{e,max} = \dot{m}_{l,max}\{c\left(T_{sat} - T_f\right) + h_{fg}\} \tag{7}$$

where c is the liquid specific heat and h_{fg} the latent heat.

The $Q_{e,max}$ and $Q'_{e,max}$ values at each δ are shown in Fig. 9 with the ratios, η and η', defined by

$$\eta = \frac{Q_{e,max}}{Q_{e,max}\big|_{\delta=1.0\text{mm}}}, \eta' = \frac{Q'_{e,max}}{Q'_{e,max}\big|_{\delta=1.0\text{mm}}} \tag{8}$$

where $Q_{e,max}\big|_{\delta=1.0\text{mm}}$ and $Q'_{e,max}\big|_{\delta=1.0\text{mm}}$ are the $Q_{e,max}$ and $Q'_{e,max}$ values for the wick structure of $\delta = 1.0$ mm, respectively. Some differences were found between the $Q_{e,max}$ and $Q'_{e,max}$ values, but η agreed with η' for $\delta = 0.5$ mm. This agreement implies that the change in $Q_{e,max}$ was proportional to δ in the range of $\delta = 0.5 - 1.0$ mm. However, such a change was not obtained in $\delta = 1.0 - 1.5$ mm. The amount of liquid rising in the wick structure increases in proportion to δ . However, vapor bubbles generated by boiling in the wick structure may block the liquid supply from the wick's thickness direction to the evaporation surface. Because of this, when $\delta = 1.5$ mm, an increment in ΔT from $Q_e = 15.9$ W to $Q_e = 17.4$ W was apparently larger in Fig. 8, and η was smaller than η' in Fig. 9.

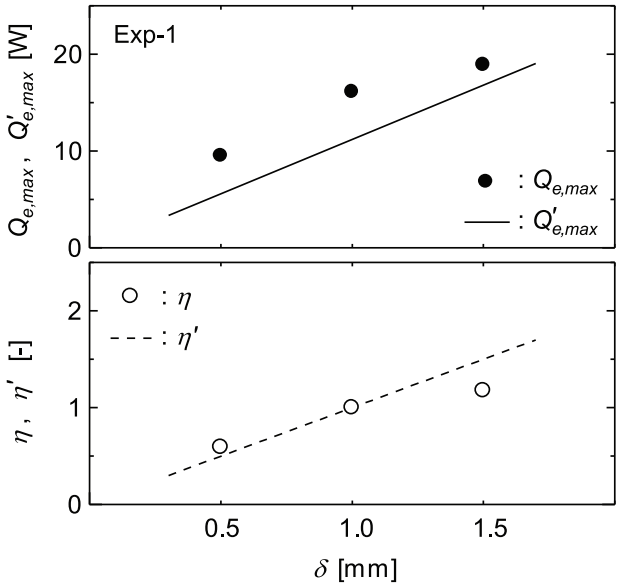

Figure 9: Maximum heat transfer rates for the 0.5, 1.0, and 1.5-mm-thick wick structures (Exp-1)

3.3 Heat Transfer Characteristics: Exp-2

Fig. 10 shows the ΔT values at each Q_l for the 1.0-mm-thick wick structure. The experimental results with the Type A and Type B additional components are compared in this figure. Since no heat was transferred from the wick structure to the right rod, Q_l was employed instead of Q_e for the horizontal axis in this figure. The heat transfer from the right surface of the wick structure to the right rod was blocked by the Type A component, whereas the vapor channel of the Type B component enabled the heat transfer from the right surface of the wick structure to atmosphere. For a low Q_l where ΔT was below a few degrees, almost no evaporation of the working fluid occurred. Besides, in case of the Type B component, the right surface of the wick structure was naturally cooled by air. Thus, for a low Q_l, the ΔT value at each Q_l with the Type B component was apparently smaller than that with the Type A component. In contrast, for a higher Q_l, it was found that a difference in the ΔT values for the two cases was small although the evaporation surface area in case of the Type B component was much larger than that of the Type A component. This agreement implies that the heat transfer from the wick structure to the atmosphere was dominated by the evaporation of the working fluid from the thin sides of the wick structure. For a higher Q_l, sufficient evaporation occurred from the thin sides of the wick structure even if the wick structure was sandwiched between the solid walls.

Regarding the relation between ΔT and Q_l for the 1.0-mm-thick wick structure, the experimental results for Exp-2 with the Type A component were compared in Fig. 11 with those for Exp-1. Because of the heat transfer from the wick structure to the right rod, the ΔT value at each Q_l for Exp-1 was entirely smaller than that for Exp-2 with Type A. Using Q_e instead of Q_l, the ΔT value for Exp-1 is replotted in Fig. 12, and compared with the relation between ΔT and Q_l for Exp-2 with Type A. Fairly good agreement was obtained between the two experimental results. Thus, the heat transfer from the wick structure to the right rod needed to be considered. The evaporation heat transfer characteristics for Exp-1 and Exp-2 with Type A were essentially the same when the net heat transfer rate was considered by Eq. (4).

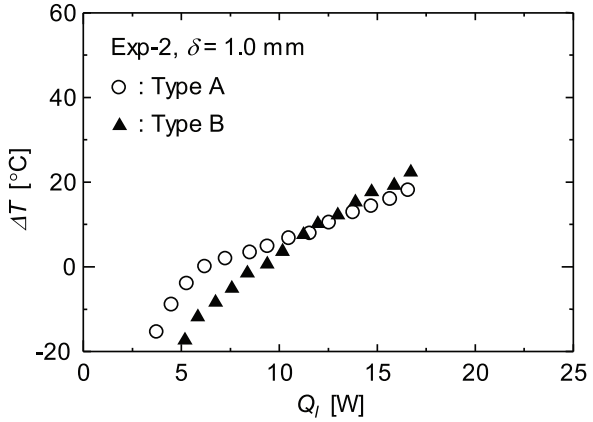

Figure 10: Comparison between the evaporation heat transfer characteristics with the Type A and Type B components (Exp-2)

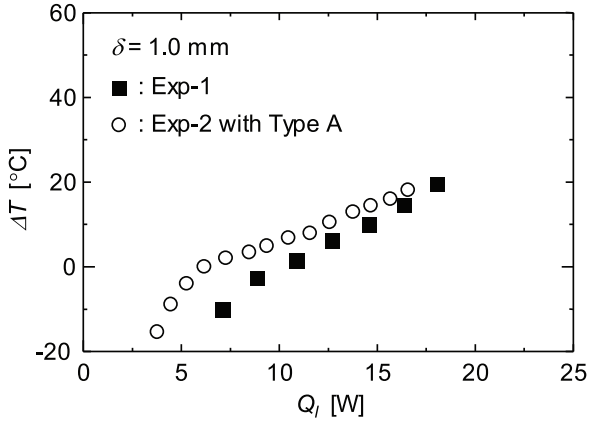

Figure 11: Comparison between the evaporation heat transfer characteristics for Exp-1 and Exp-2 with the Type A component (plotted with Q_l)

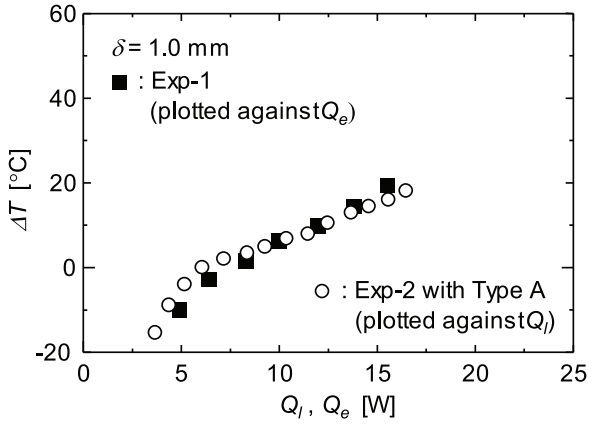

Figure 12: Comparison between the evaporation heat transfer characteristics for Exp-1 and Exp-2 with the Type A component (plotted with Q_e for Exp-1 and Q_l for Exp-2)

4 Conclusions

Evaporation heat transfer characteristics from the wick structure sandwiched between the solid walls were investigated experimentally. The 0.5, 1.0, and 1.5-mm-thick strip-shaped wick structures made of sintered copper powder were employed with water as the working fluid. The capillary pumping performance, that is, the liquid lifting velocities of the three wick structures were the same. The findings obtained in this study are summarized as follows:

- When the wick's thickness was reduced from 1.0 to 0.5 mm, the maximum heat transfer rate decreased in proportion to the thickness. However, the evaporation thermal resistances were almost the same for the two wick structures.
- When the wick's thickness was increased from 1.0 to 1.5 mm, the maximum heat transfer rate increased. However, such a proportional change was not obtained for the 1.5-mm-thick wick structure.
- Even if the wick structure was sandwiched between the solid walls, sufficient evaporation occurred from the wick structure.
- Regardless of the heat transfer from the wick structure to the right rod, the heat transfer characteristics were essentially the same when the net heat transfer rate was considered.

Acknowledgement: The authors would like to thank Mr. Kenya Haraguchi and Mr. Koki Fukamizu for useful discussions.

Funding Statement: The authors received no specific funding for this study.

Author Contributions: The authors confirm contribution to the paper as follows: study conception and design: Y. Koito; data collection: S. Hitotsuya, T. Takayama, K. Hashimoto; analysis and interpretation of results: Y. Koito, S. Hitotsuya, T. Takayama, K. Hashimoto; draft manuscript preparation: Y. Koito. All authors reviewed the results and approved the final version of the manuscript.

Availability of Data and Materials: The data are available from the corresponding author upon reasonable request.

Conflicts of Interest: The authors declare that they have no conflicts of interest to report regarding the present study.

References

1. Tang, H., Tang, Y., Wan, Z., Li, J., Yuan, W. et al. (2018). Review of applications and developments of ultra-thin micro heat pipes for electronic cooling. *Applied Energy, 223,* 383–400.
2. Mochizuki, M., Nguyen, T. (2019). Review of various thin heat spreader vapor chamber designs, performance, lifetime reliability and application. *Frontiers in Heat and Mass Transfer, 13,* 12.
3. Velardo, J., Singh, R., Ahamed, M. S., Mochizuki, M., Date, A. et al. (2021). Thin thermal management modules using flattened heat pipes and piezoelectric fans for electronic devices. *Frontiers in Heat and Mass Transfer, 17,* 1.
4. Wang, Y., Wang, J., He, X., Duan, J. (2021). Experimental investigation of the thermal performance of a heat sink with U-shaped heat pipes. *Applied Thermal Engineering, 186,* 116387.

5. Zhao, J., Du, M., Zhang, Z., Ling, X. (2021). Thermal management strategy for electronic chips based on combination of a flat-plate heat pipe and spray cooling. *International Journal of Heat and Mass Transfer, 181,* 121894.
6. Singh, R., Mochizuki, M., Yamada, T., Nguyen, T. (2020). Cooling of led headlamp in automotive by heat pipes. *Applied Thermal Engineering, 166,* 114733.
7. Pekur, D. V., Sorokin, V. M., Nikolaenko, Y. E. (2020). Thermal characteristics of a compact LED luminaire with a cooling system based on heat pipes. *Thermal Science and Engineering Progress, 18,* 100549.
8. Tang, Y., Luo, Y., Du, P., Wang, H., Ma, H. et al. (2021). Experimental investigation on active heat sink with heat pipe assistance for high-power automotive LED headlights. *Case Studies in Thermal Engineering, 28,* 101503.
9. Behi, H., Behi, M., Karimi, D., Jaguemont, J., Ghanbarpour, M. et al. (2021). Heat pipe air-cooled thermal management system for lithium-ion batteries: High power applications. *Applied Thermal Engineering, 183(2),* 116240.
10. Luo, Y., Tang, Y., Zhang, X., Wang, H., Zhou, G. et al. (2022). A novel composite vapor chamber for battery thermal management system. *Energy Conversion and Management, 254,* 115293.
11. Tang, Y., Deng, D., Lu, L., Pan, M., Wang, Q. (2010). Experimental investigation on capillary force of composite wick structure by ir thermal imaging camera. *Experimental Thermal and Fluid Science, 34(2),* 190–196.
12. Weibel, J. A., Garimella, S. V., North, M. T. (2010). Characterization of evaporation and boiling from sintered powder wicks fed by capillary action. *International Journal of Heat and Mass Transfer, 53(19–20),* 4204–4215.
13. Weibel, J. A., Garimella, S. V. (2012). Visualization of vapor formation regimes during capillary-fed boiling in sintered-powder heat pipe wicks. *International Journal of Heat and Mass Transfer, 55(13–14),* 3498–3510.
14. Deng, D., Tang, Y., Huang, G., Lu, L., Yuan, D. (2013). Characterization of capillary performance of composite wicks for two-phase heat transfer devices. *International Journal of Heat and Mass Transfer, 56(1–2),* 283–293.
15. Sudhakar, S., Weibel, J. A., Garimella, S. V. (2019). Experimental investigation of boiling regimes in a capillary-fed two-layer evaporator wick. *International Journal of Heat and Mass Transfer, 135,* 1335–1345.
16. Zhang, S., Chen, C., Chen, G., Sun, Y., Tang, Y. et al. (2020). Capillary performance characterization of porous sintered stainless steel powder wicks for stainless steel heat pipes. *International Communications in Heat and Mass Transfer, 116,* 104702.
17. Koito, Y. (2019). Numerical analyses on heat transfer characteristics of ultra-thin heat pipes: Fundamental studies with a three-dimensional thermal-fluid model. *Applied Thermal Engineering, 148,* 430–437.
18. Zhou, W., Li, Y., Chen, Z., Deng, L., Li, B. (2020). Experimental study on the heat transfer performance of ultra-thin flattened heat pipe with hybrid spiral woven mesh wick structure. *Applied Thermal Engineering, 170,* 115009.
19. Tang, H., Weng, C., Tang, Y., Li, H., Xu, T. et al. (2021). Thermal performance enhancement of an ultra-thin flattened heat pipe with multiple wick structure. *Applied Thermal Engineering, 183(1),* 116203.
20. Faghri, A. (2016). *Heat pipe science and technology*. 2nd edition. USA: Global Digital Press.
21. Li, Y., He, J., He, H., Yan, Y., Zeng, Z. et al. (2015). Investigation of ultra-thin flattened heat pipes with sintered wick structure. *Applied Thermal Engineering, 86,* 106–118.
22. Ahamed, M. S., Saito, Y., Mashiko, K., Mochizuki, M. (2017). Characterization of a high performance ultra-thin heat pipe cooling module for mobile hand held electronic devices. *Heat and Mass Transfer, 53(11),* 3241–3247.
23. Yang, K. S., Tu, C. W., Zhang, W. H., Yeh, C. T., Wang, C. C. (2017). A novel oxidized composite braided wires wick structure applicable for ultra-thin flattened heat pipes. *International Communications in Heat and Mass Transfer, 88,* 84–90.

24. Zhou, W., Xie, P., Li, Y., Yan, Y., Li, B. (2017). Thermal performance of ultra-thin flattened heat pipes. *Applied Thermal Engineering, 117,* 773–781.
25. Dai, X., Tang, Y., Liu, T., Wang, S. (2020). Experimental investigation on the thermal characteristics of ultra-thin flattened heat pipes with bending angles. *Applied Thermal Engineering, 172,* 115150.
26. Li, D., Huang, Z., Liao, X., Zu, S., Jian, Q. (2021). Heat and mass transfer characteristics of ultra-thin flat heat pipe with different liquid filling rates. *Applied Thermal Engineering, 199,* 117588.
27. Liao, X., Jian, Q., Zu, S., Li, D., Huang, Z. (2021). Visualization study and analysis on the heat transfer performance of an ultra-thin flat-plate heat pipe. *International Communications in Heat and Mass Transfer, 126,* 105464.
28. Lv, L., Li, J. (2017). Managing high heat flux up to 500 W/cm^2 through an ultra-thin flat heat pipe with superhydrophilic wick. *Applied Thermal Engineering, 122,* 593–600.
29. Li, J., Lv, L., Zhou, G., Li, X. (2019). Mechanism of a microscale flat plate heat pipe with extremely high nominal thermal conductivity for cooling high-end smartphone chips. *Energy Conversion and Management, 201,* 112202.
30. Cui, Z., Jia, L., Wang, Z., Dang, C., Yin, L. (2022). Thermal performance of an ultra-thin flat heat pipe with striped super-hydrophilic wick structure. *Applied Thermal Engineering, 208,* 118249.
31. Joint Committee for Guides in Metrology (2008). *Evaluation of measurement data-Guide to the expression of uncertainty in measurement*.

Appendix. Derivation process of Eq. (2)

Regarding the height, h, of the liquid rising in the wick structure, the following equation was obtained from the equation of motion:

$$\rho_l A\varepsilon \frac{d}{dt}\left(h\frac{dh}{dt}\right) = F - A\frac{\mu_l}{K}h\frac{dh}{dt} - \rho_l A\varepsilon hg \tag{A-1}$$

where ρ_l is the liquid density, A the cross-sectional area of the wick structure, ε the porosity of the wick structure, F the capillary force of the wick structure, μ_l the liquid viscosity, K the permeability of the wick structure, and g the gravitational acceleration. The flow resistance in the wick structure was considered in the second term on the right side of Eq. (A-1) using Darcy's law, and the influence of the gravity was considered in the third term. Eq. (2) was obtained by using X_1 and X_2 defined by the following equations:

$$X_1 = \frac{F}{\rho_l A\varepsilon}, X_2 = \frac{\mu_l}{\rho_l \varepsilon K} \tag{A-2}$$

The temporal change in h was obtained numerically from Eqs. (A-1) and (A-2) with X_1 and X_2 as parameters. By comparing the numerical results with the experimental results, the X_1 and X_2 values were determined as shown in Eq. (2).